Supplementary information

A Multifunctional Natural Clay Mineral Additive for Stabilizing Ni-Rich Layered Oxide Cathodes

Liu Yang[a, d, #], Zeyi Wang[c, #], Lu Chen[a], Yanxin Jiang[a], Hongji Pan[a, *], Chunlei Song[a], Tianshuai Wang[c, *], Anjun Hu[d], Jianping Long[d, *], Yiju Li[a, b, *], Tianshou Zhao[a, b]

[a.] *Department of Mechanical and Energy Engineering, Southern University of Science and Technology, Shenzhen, 518055, P.R. China*
[b.] *SUSTech Energy Institute for Carbon Neutrality, Southern University of Science and Technology, Shenzhen, 518055, P.R. China*
[c.] *Xi'an Key Laboratory of Functional Organic Porous Materials, School of Chemistry and Chemical Engineering, Northwestern Polytechnical University, Xi'an, 710129, China*
[d.] *College of Materials and Chemistry & Chemical Engineering (College of Lithium Resources and Lithium Battery Industry), Chengdu University of Technology, Chengdu 610059, China.*

[#] *These authors contributed equally*

E-mail: liyj6@sustech.edu.cn (Yiju Li); longjianping@cdut.cn (Jianping Long); tianshuai@nwpu.edu.cn (Tianshuai Wang); phj1300@163.com (Hongji Pan)

Keywords: halloysite, natural clay, eliminating transmission metal ions, lithium batteries

Experimental method

Materials and chemicals

All chemicals were of analytical grade and were used without further purification. The natural 7 Å halloysite nano clay ($Al_2Si_2O_5(OH)_4$) was purchased from Aladdin Reagent (Shanghai, China) Co., Ltd. Both the $LiNi_{0.6}Mn_{0.2}Co_{0.2}O_2$ (NCM622) and $LiNi_{0.8}Mn_{0.1}Co_{0.1}O_2$ (NCM811) cathode materials used in this study were of the single-crystal type and were supplied by Guangdong Canrd New Energy Technology Co., Ltd. The commercial electrolyte of 1 M $LiPF_6$ in EC/EMC (volume ratio of 3:7) and FEC additive was purchased from DodoChem Co. and used as received. Manganese (II) bis(trifluoromethanesulfonyl)imide) and nickel (II) bis(trifluoromethanesulfonimide) additives were purchased from Aladdin Reagent (Shanghai, China) Co., Ltd.

HNT-NCM fabrication

The HNTs used in this study were commercially sourced from Aladdin. Before use, the HNT powder was purified by stirring in a 0.3 mmol L^{-1} HCl aqueous solution at 70 °C for 2 h. After the acid treatment, the sample was thoroughly washed with deionized water more than three times until the supernatant reached a neutral pH. The purified solid was then collected by centrifugation and annealed in air at 180 °C for 12 h to remove residual moisture. For the preparation of HNT-NCM622 (donated as HNT-NCM), three different mass ratios of HNT (100 mg [1 wt.%], 300 mg [3 wt.%], or 500 mg [5 wt.%]) were thoroughly mixed with 10 g of $LiNi_{0.6}Mn_{0.2}Co_{0.2}O_2$ (NCM622) cathode material. The mixtures were then subjected to ball milling using zirconia grinding media at a mass ratio of 1:8 (composite material to grinding media) for 10 min at a relatively mild speed of 500 rpm, using a mini-type ball mill. These conditions were carefully chosen to ensure uniform mixing without inducing structural pulverization or damaging the NCM622 particles, as verified by subsequent SEM characterization.

Electrode preparation and TMs-containing electrolyte fabrication

HNT-NCM cathode with a capacity of 0.6 mAh cm^{-2} was prepared by mixing 80 wt.% HNT-NCM material, 10 wt.% Super P and 10 wt.% polyvinylidene fluoride (PVDF) binder slurry in N-methyl-2pyrrolidone (NMP) solvent. The resulting slurry was cast on the Al foil and then dried at 80 °C for 12 h in a vacuum oven. A solution of 8 mM Mn $(TFSI)_2$/Ni $(TFSI)_2$ in 1 M $LiPF_6$ in EC/EMC (3:7 v/v) was prepared by dissolving 25 mg Mn $(TFSI)_2$/Ni $(TFSI)_2$ in 5 mL of the electrolyte solvent.

General characterization

The crystallographic structure of the cathodes after cycling was identified via a Bruker D8 Advance

diffractometer (2θ collected from 10-80°, with a scan rate of 2° min^{-1}). The field-emission SEM (TESCAN Brno, s.r.o., MAIA3) and HR-TEM (FEI Talos F200X) were used to confirm the morphology and element distribution of as-prepared cathode samples. The chemical composition of the cathode electrode interface was conducted using X-ray photoelectron spectrometry measurements (PerkinElmer PHI 1600 ESCA). The content and distribution of TMs and byproduct fragments on cycled lithium metal were characterized using ToF-SIMS (ION-TOF GmbH).

Electrochemical test

All batteries were assembled in the Argon-filled glove box ($H_2O \leq 0.01$ ppm, $O_2 \leq 0.01$ ppm). For the NCM//Li and HNT-NCM//Li half cells, the pre-weighed cathode and a 16 mm Celgard PP separator are sequentially assembled into CR2032 coin cells, followed by the injection of 80 μL of electrolyte. Subsequently, a 100 μm-thick lithium metal layer is placed onto the PP separator. The assembled half batteries were rested for 2 hours before the electrochemical test. The cut-off voltage was from 2.0 V to 3.0 V. The electrochemical test was conducted in the voltage range of 2.7-4.3 V on a LAND Battery tester. In situ electrochemical impedance (in situ EIS) of the cells was performed on the CHI920D Electrochemical workstation (Chenhua, Shanghai) with a frequency range from 10^5 to 10^{-2} Hz at 25 °C. The GITT is performed at 0.1 C between 2.7 V and 4.3 V, with a constant current pulse of 10 minutes and a relaxation step of 30 minutes. The HNT-NCM//Li full coin cell was assembled using ultrathin Li foil (50 μm), an HNT-NCM cathode with a mass loading of 22.9 mg cm^{-2}, a PP separator, and 1 M $LiPF_6$ in EC/EMC (3:7 v/v) with 10 vol% FEC as the liquid electrolyte. For the HNT-NCM//Gr full cells with a cathode loading of 17.2 mg cm^{-2}, the graphite electrodes with an areal capacity of 3.0 mAh cm^{-2} and a PP separator were used as the anode and separator, respectively (electrolyte: 1 M $LiPF_6$ in EC/EMC (3:7 v/v) or 1 M $LiPF_6$ in EC/EMC (3:7 v/v) with 10 vol% FEC). The HNT-NCM//Li pouch cells (60.8 mAh, cathode capacity: 3.8 mAh cm^{-2}, electrolyte: 1 M $LiPF_6$ in EC/EMC (3:7 v/v) with 10 vol% FEC, 3.0 g Ah^{-1}) were assembled in an argon-filled glove box.

Theoretical calculation

Spin-polarized density functional theory (DFT) calculations were performed using the Vienna Ab initio Simulation Package (VASP) with the projector augmented wave (PAW) method and plane-wave basis sets. The exchange-correlation interactions were described using the generalized gradient approximation (GGA) with the Perdew-Burke-Ernzerhof (PBE) functional. A plane-wave kinetic energy cutoff of 500 eV was employed throughout all calculations. To better account for the localized 3d electrons, the Hubbard U correction (PBE+U) was applied with effective U values of 3.9 eV for Mn, 3.4 eV for Co, and 6.0 eV for Ni, respectively. Dispersion interactions were considered using the DFT-D3 method with Becke-Johnson

damping. The Brillouin zone was sampled using the Monkhorst-Pack scheme with a k-point mesh of 3 × 2 × 1 in the Gamma-centered grids for the structural relaxation. The structures were fully relaxed until the maximum force on each atom was less than 0.01 eV/Å, and the energy convergence standard was 10^{-5} eV. The adsorption energy is calculated according to the following equation:

$$E_{ads} = E_{total} - E_{HNT} - E_{species}$$

Where E_{total}, E_{HNT}, and $E_{species}$ represent the total energy of the system, the energy of the 7 Å HNT, and the energy of the species, respectively.

For the diffusion barrier calculations, a 1×1×1 k-point mesh was used. The diffusion barriers for Li atoms on the catalysts were calculated using the climbing-image nudged elastic band (CI-NEB) method.

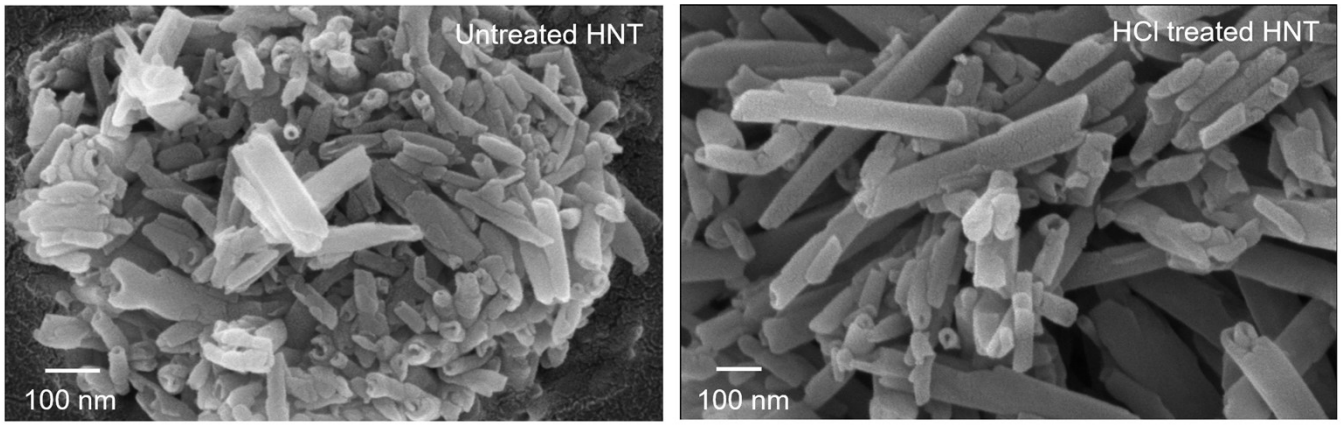

Figure S1. SEM images of HNT before and after treatment with HCl.

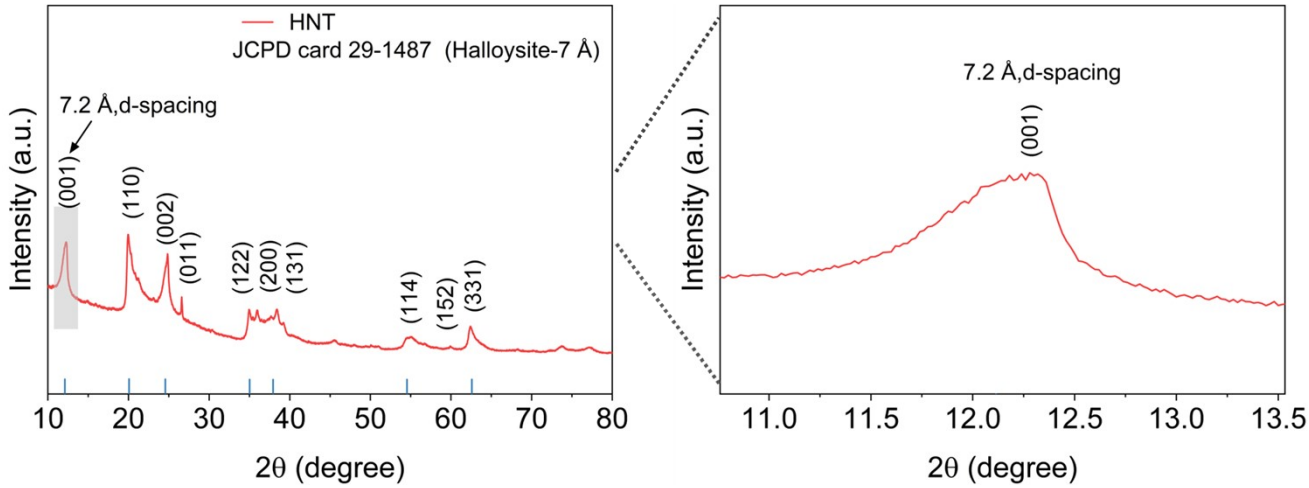

Figure S2. XRD patterns of the HNT.

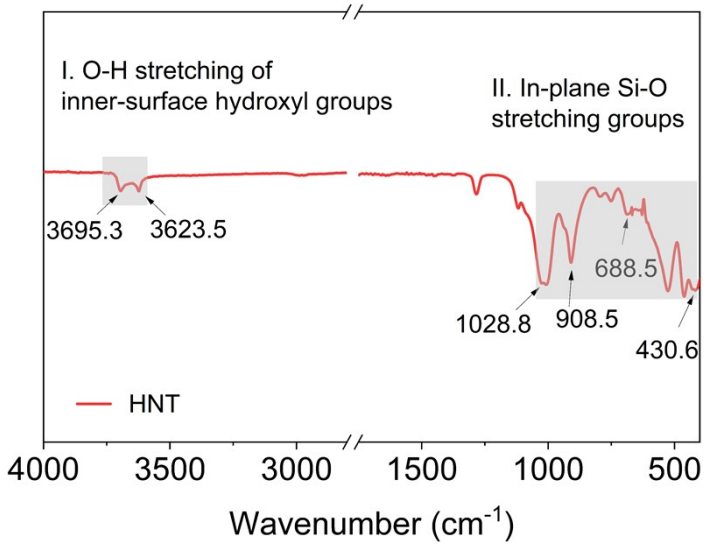

Figure S3. FT-IR patterns of the HNT.

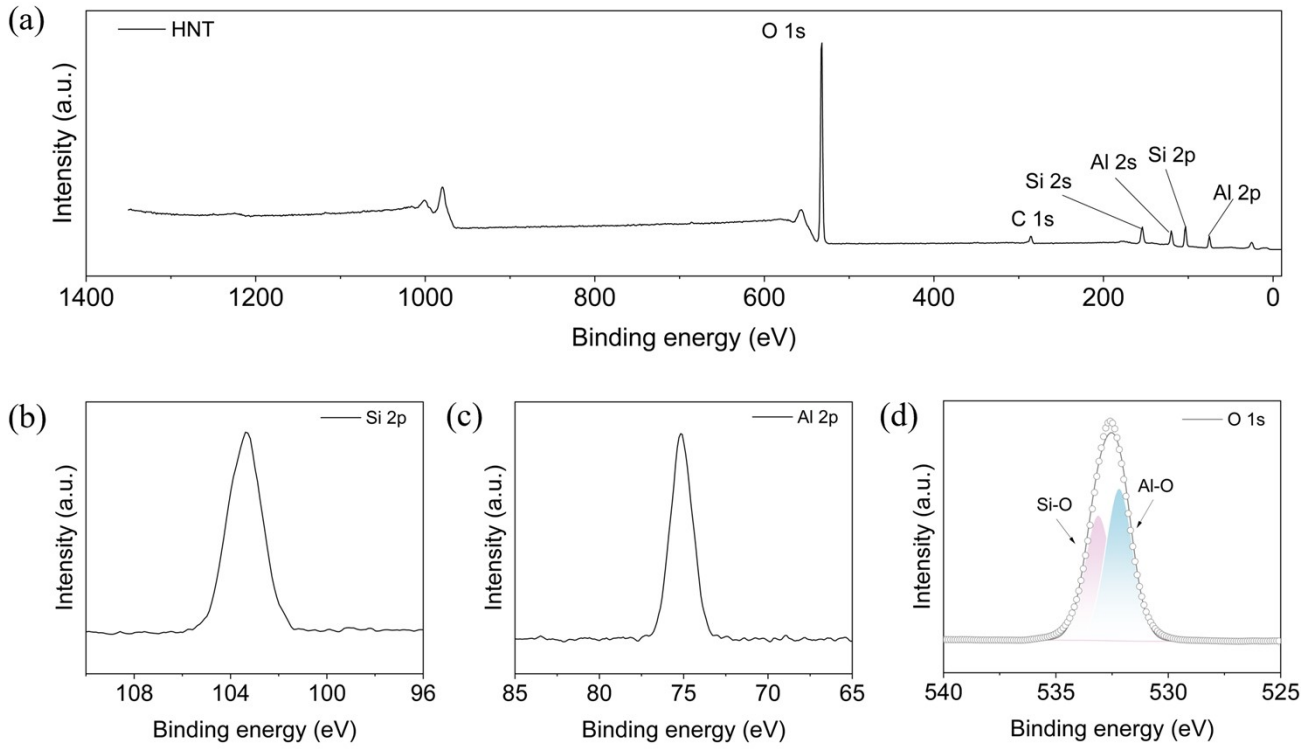

Figure S4. Survey of XPS spectra of HNT, (b) Detailed Si 2p XPS spectra of HNT, (c) Detailed Al 2p XPS spectra of HNT, (d) Detailed O 1s XPS spectra of HNT.

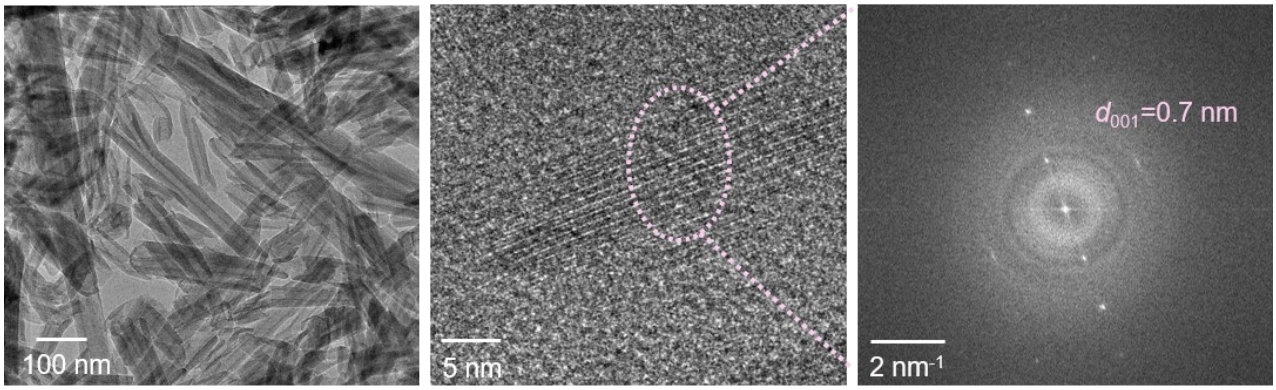

Figure S5. HR-TEM image of 7 Å halloysite and corresponding FFT image.

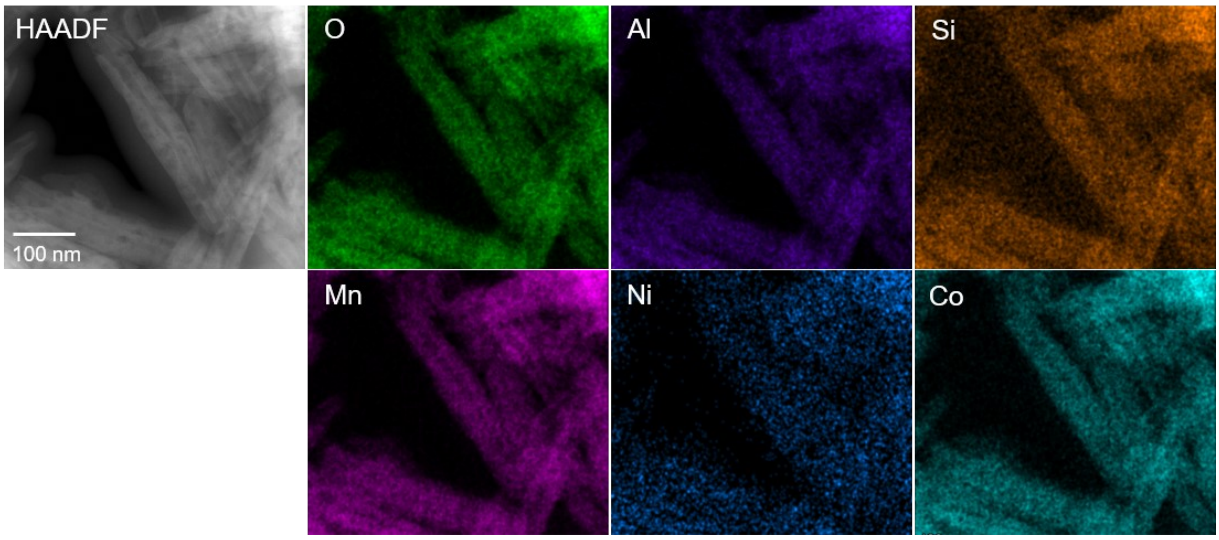

Figure S6. EDS mapping image for HNT after absorbing Mn^{2+}, Ni^{2+}, and Co^{2+}.

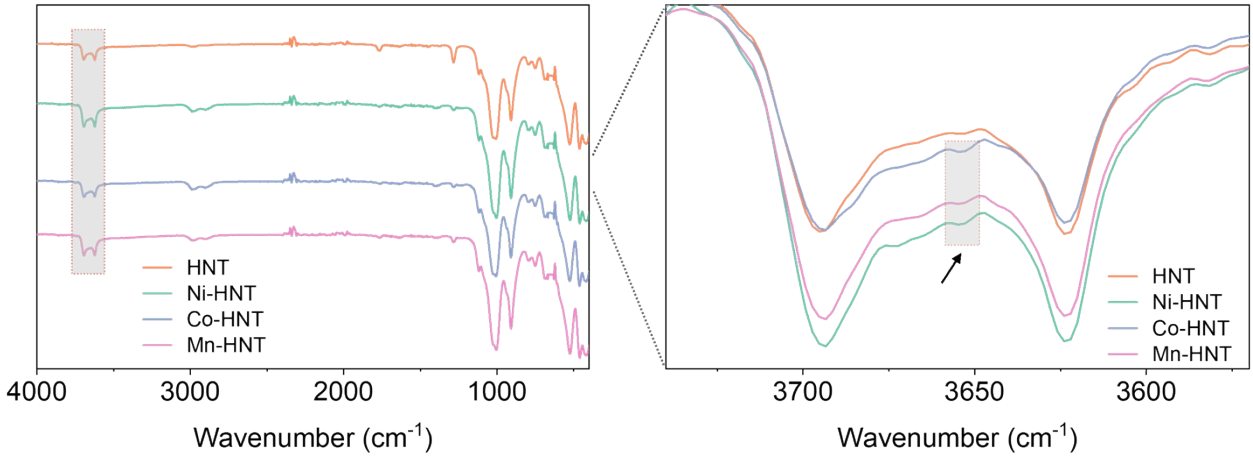

Figure S7. FT-IR spectra of HNT, Ni-HNT, Co-HNT, and Mn-HNT.

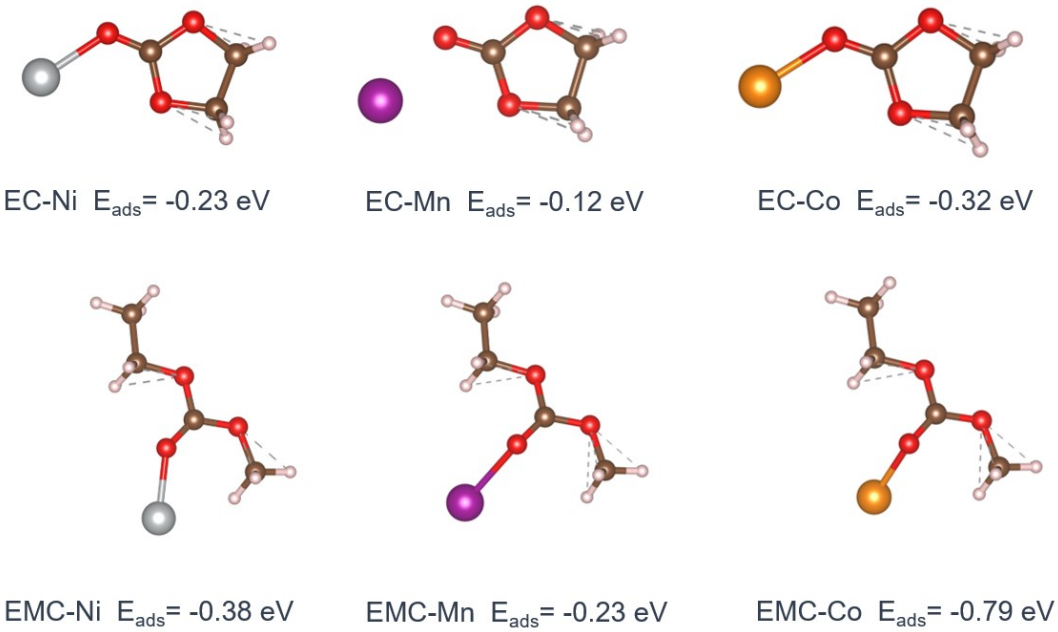

Figure S8. The calculation structure model of the absorption energies between EC/EMC and Ni^{2+}, Mn^{2+}, and Co^{2+}.

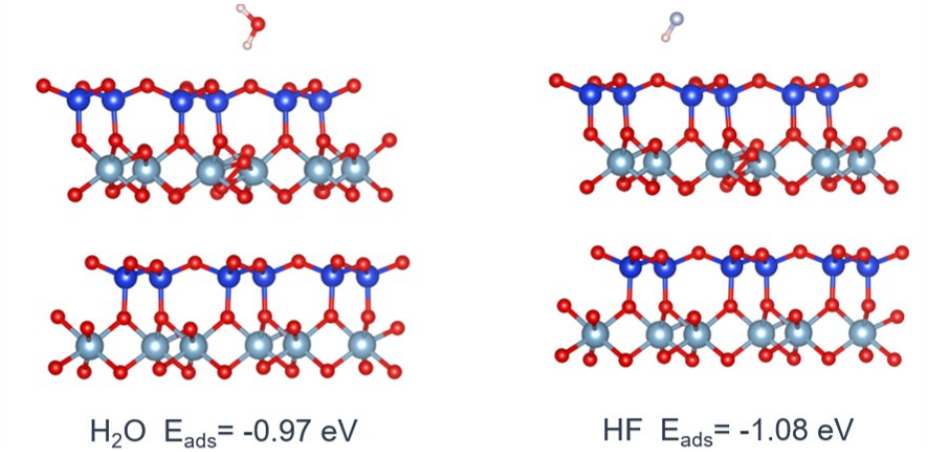

Figure S9. The calculation structure model of the absorption energies between HNT and H_2O/HF.

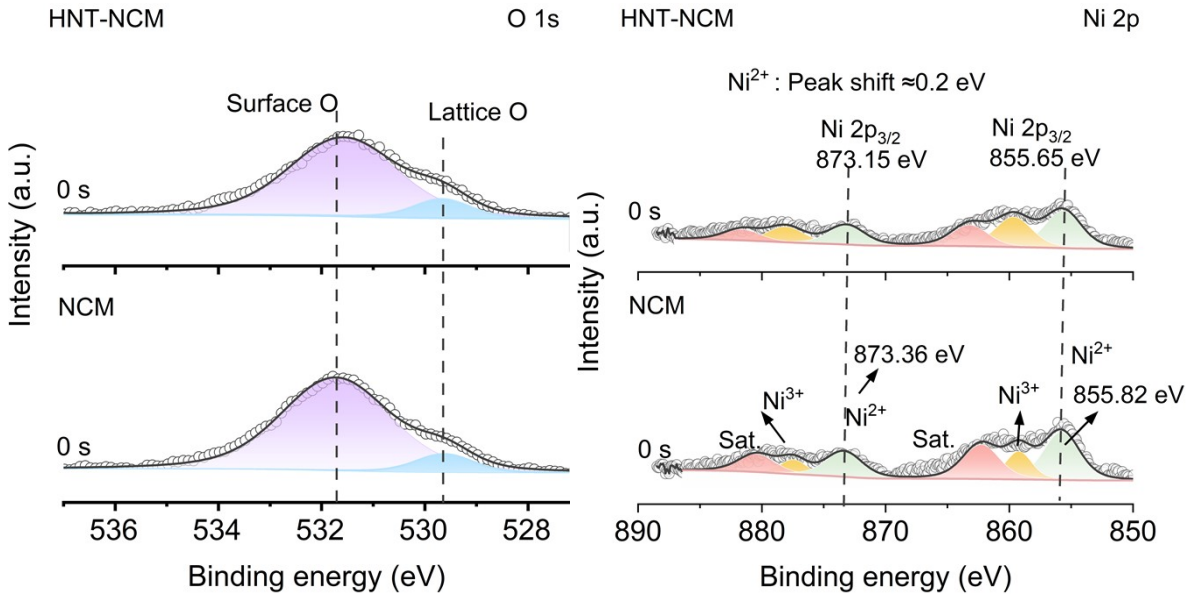

Figure S10. XPS spectra of O 1s and Ni 2p for the HNT-NCM and NCM cathode.

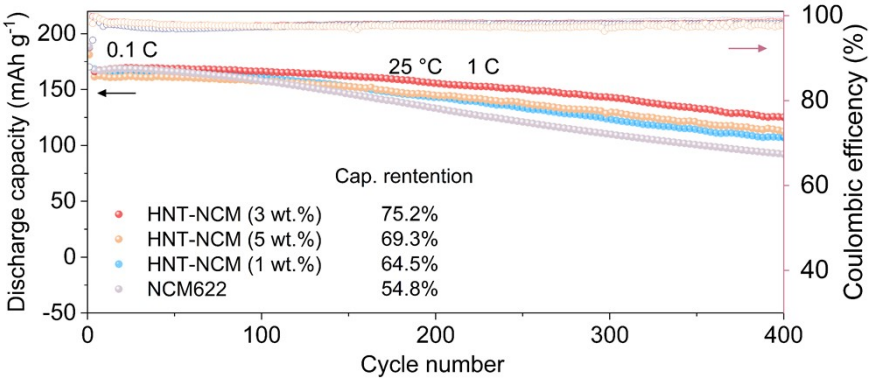

Figure S11. Long-term cycling curves of the NCM and HNT-NCM-based cell (1 wt.%, 3 wt.%, and 5 wt.%)

at 1 C, 25 °C.

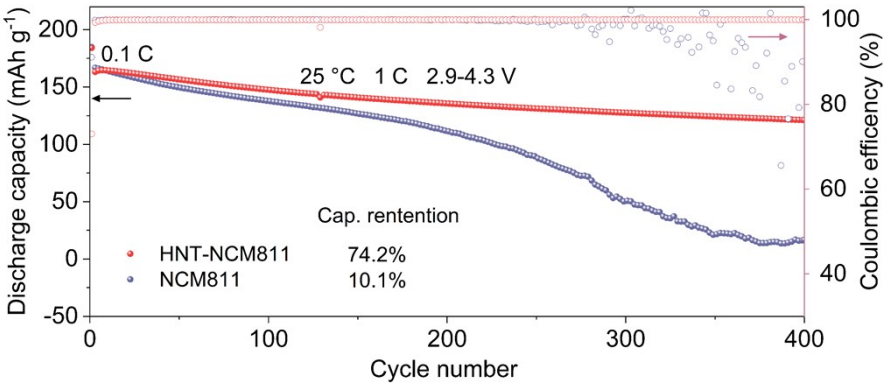

Figure S12. Cycling performance of the NCM811, HNT-NCM811-based cells at 1 C, 25 °C.

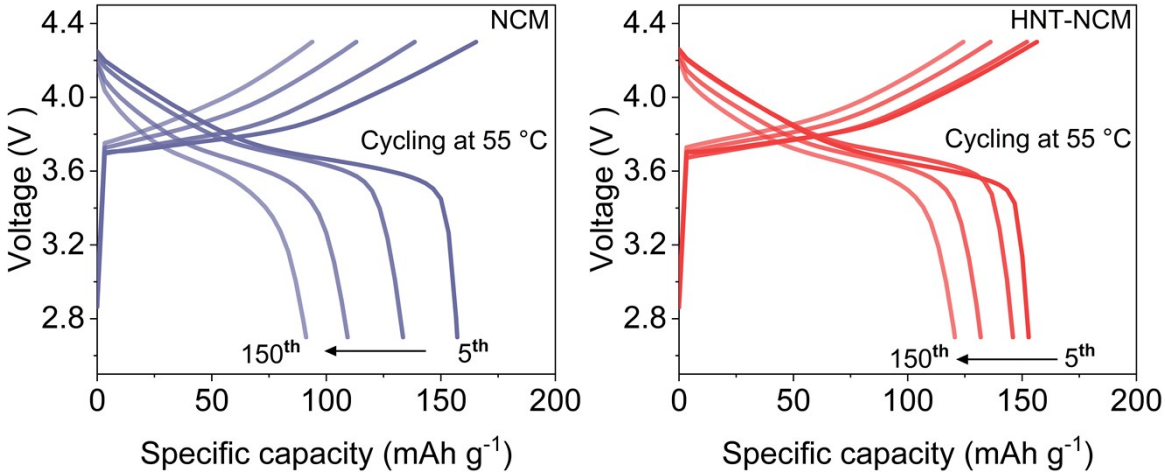

Figure S13. The charge-discharge curves of different cycles of the NCM and HNT-NCM based cell at 1 C (55 °C).

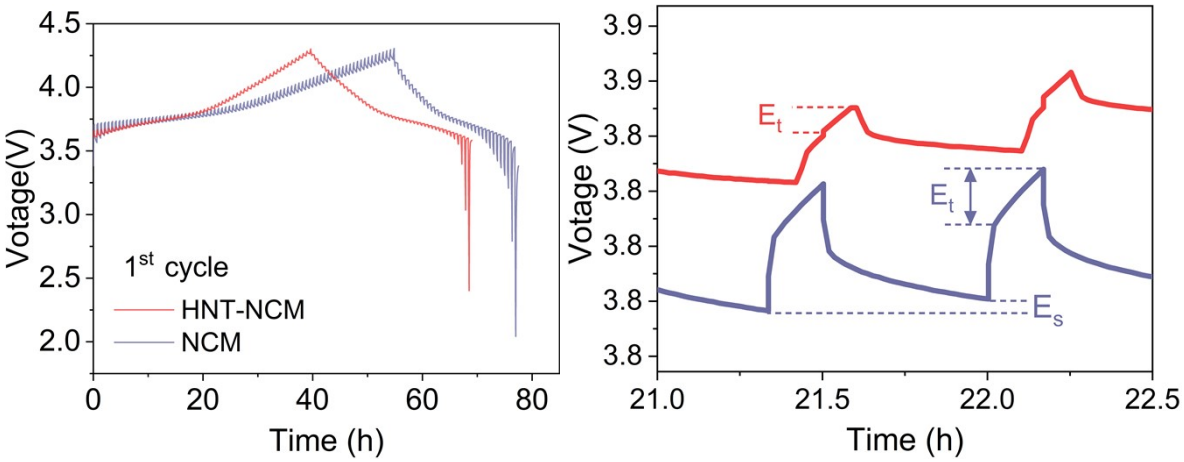

Figure S14. GITT voltage profiles of NCM and HNT-NCM-based cells during the first cycle after 10 pre-cycles.

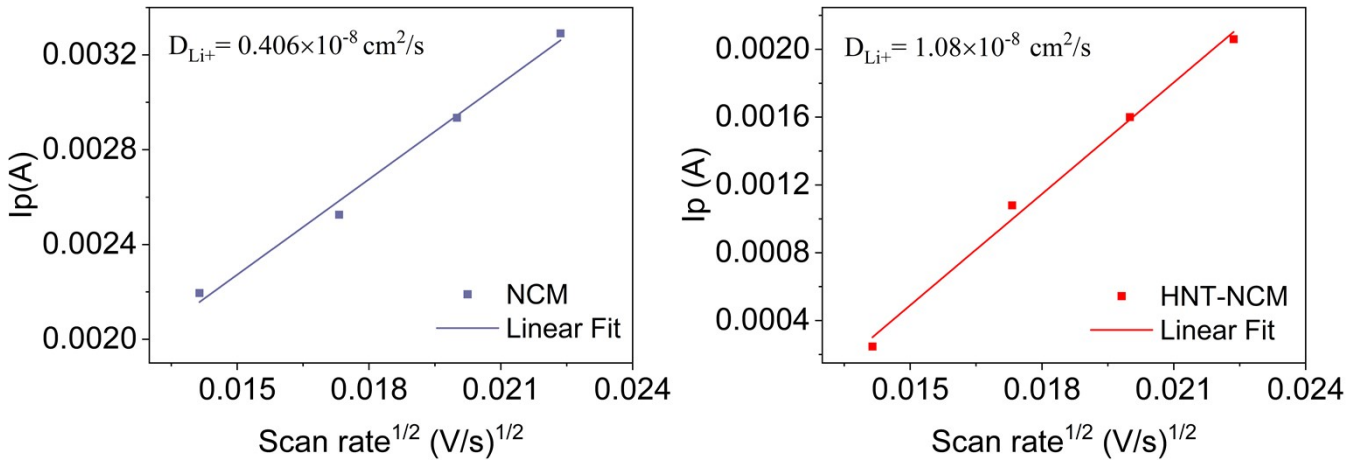

Figure S15. Fitting analysis of oxidation peak current (I_p) vs. square root of the scan rate ($v^{1/2}$).

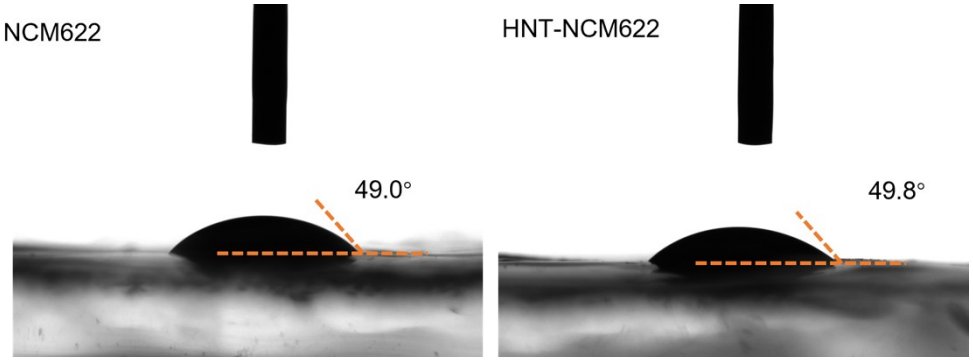

Figure S16. Contact angle images between electrolyte and cathode (NCM622 or HNT-NCM622).

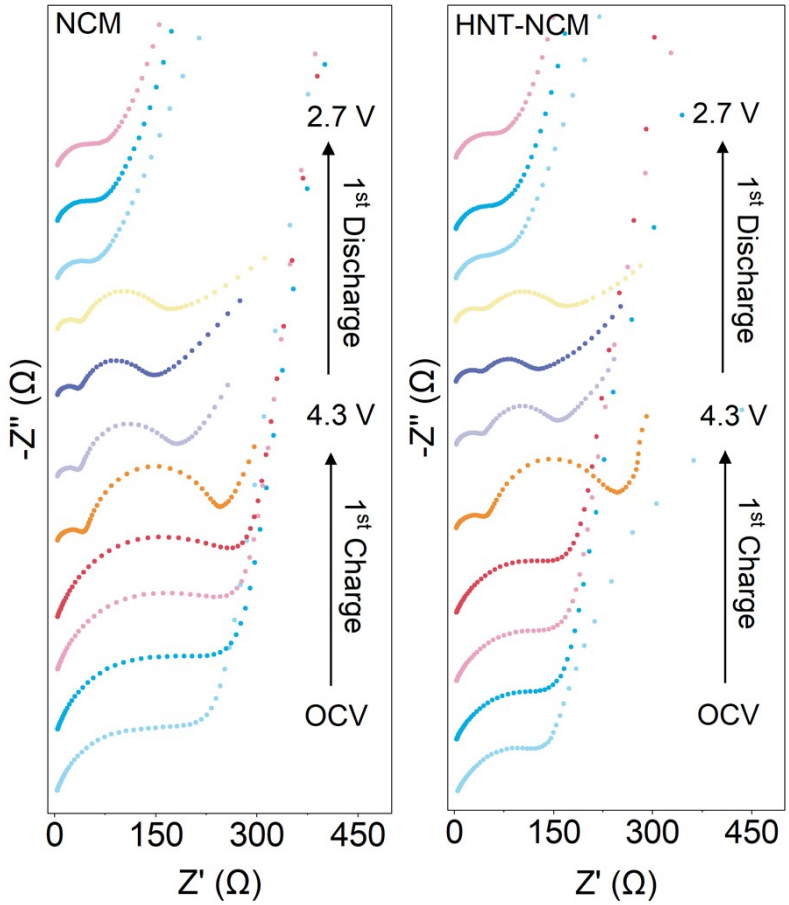

Figure S17. In situ EIS spectra of the NCM and HNT-NCM-based cell during the first charge-discharge cycle after 10 pre-cycles.

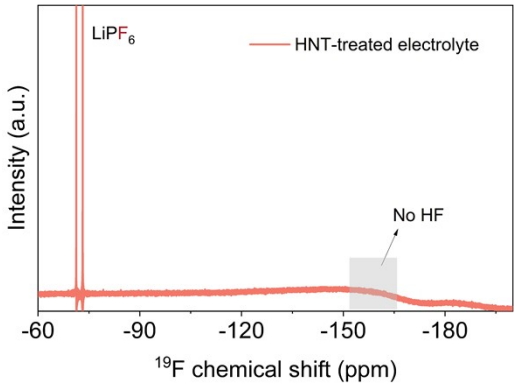

Figure S18. ^{19}F NMR spectra of the H_2O-containing electrolyte after treatment with HNT.

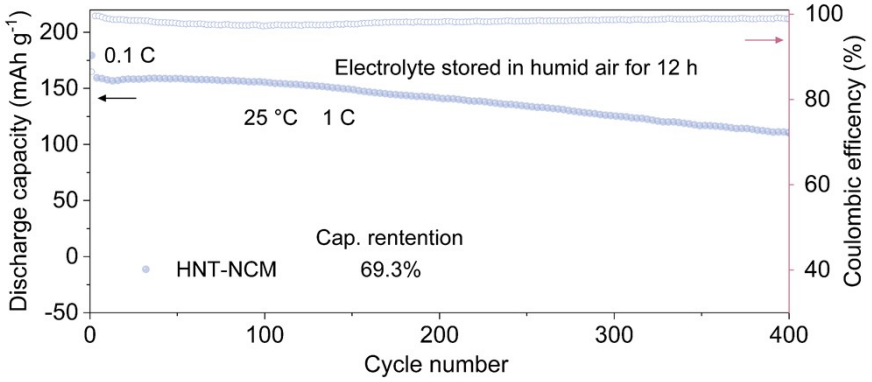

Figure S19. Cycling performance of HNT-NCM-based cell in the electrolyte after 12 h exposure to humid air (at 30 °C and 80% humidity), tested at 1 C within a voltage range of 2.7-4.3 V.

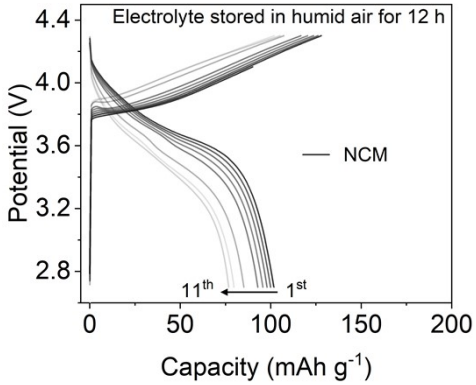

Figure S20. Charge/discharge curves of the NCM-based cell in the electrolyte after 12 h exposure to humid air (at 30 °C and 80% humidity), tested at 1 C within a voltage range of 2.7-4.3 V.

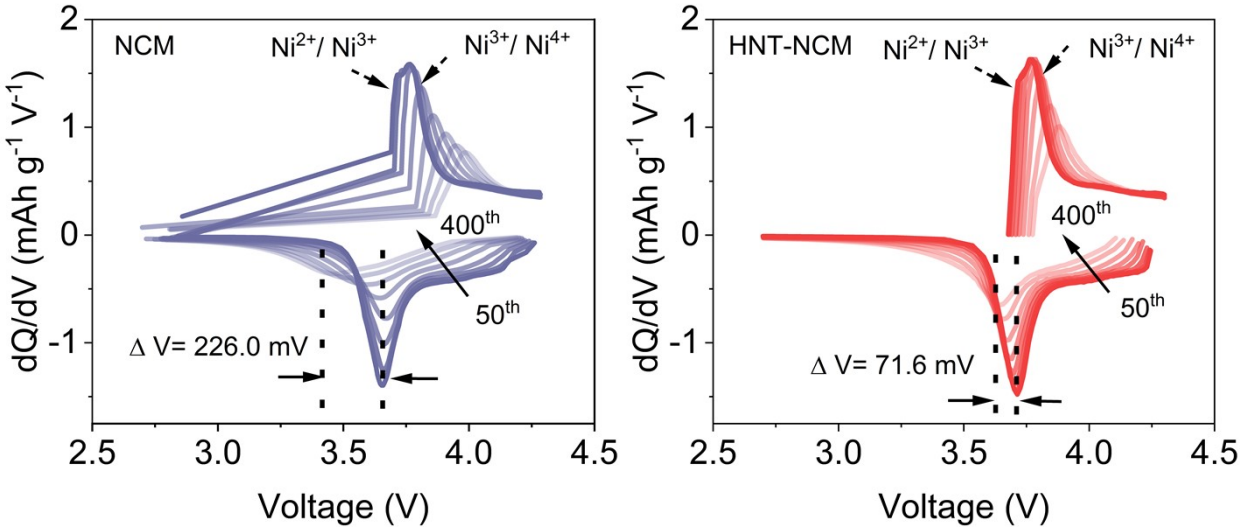

Figure S21. The dQ/dV curves of the NCM and HNT-NCM (3 wt.%) based cell with different cycles (50-400 cycles) at 2 C (25 °C).

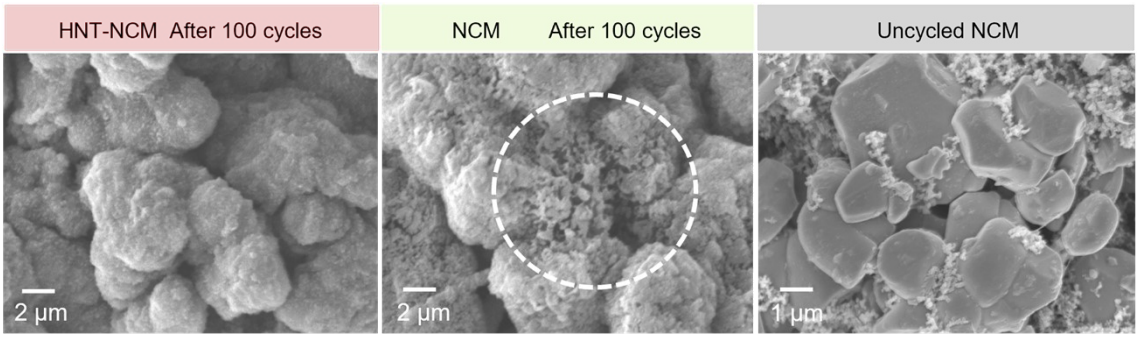

Figure S22. SEM images of the HNT-NCM, NCM cathode after 100 cycles under a 1 C rate, and SEM image of uncycled NCM cathode.

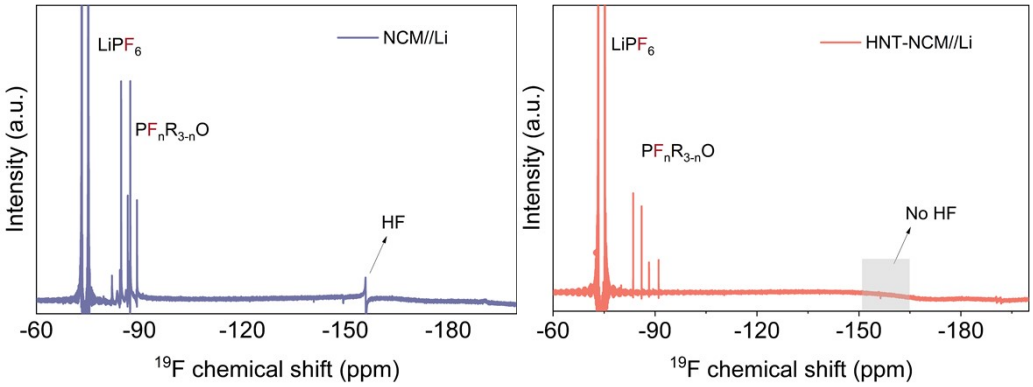

Figure S23. ^{19}F NMR spectra of the aged electrolyte from NCM//Li and HNT-NCM//Li cells after 100 cycles at 1 C.

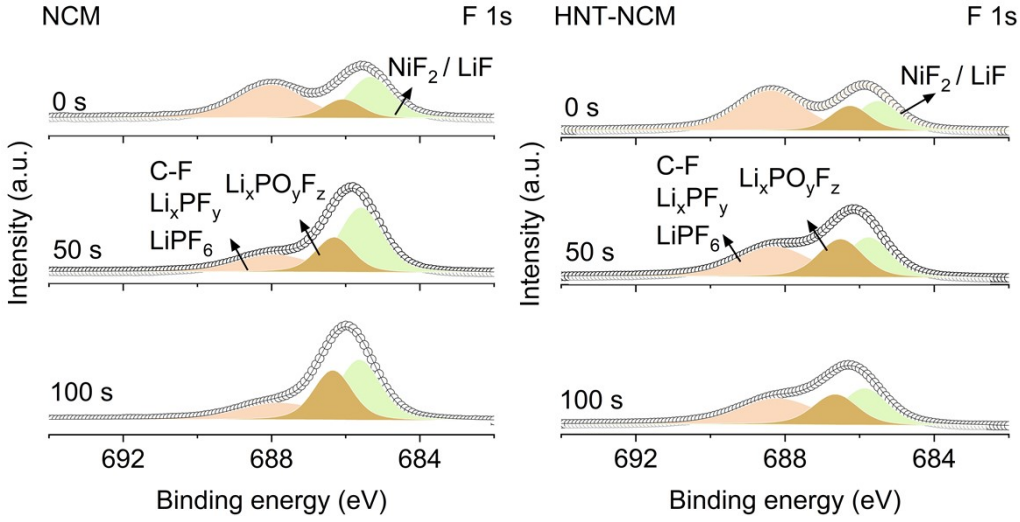

Figure S24. XPS spectra of F 1s for the NCM and HNT-NCM cathode after 100 cycles.

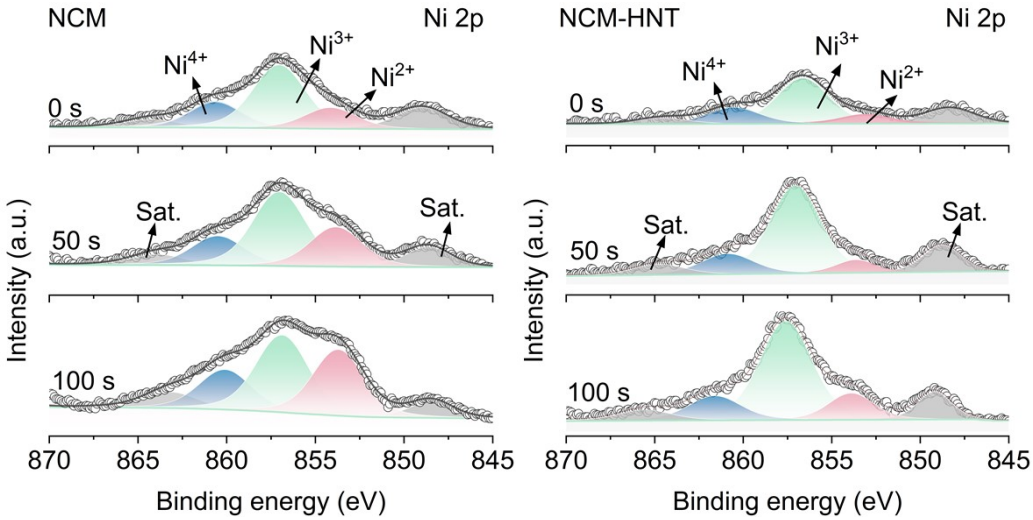

Figure S25. XPS spectra of Ni 2p for the NCM and HNT-NCM cathode after 100 cycles.

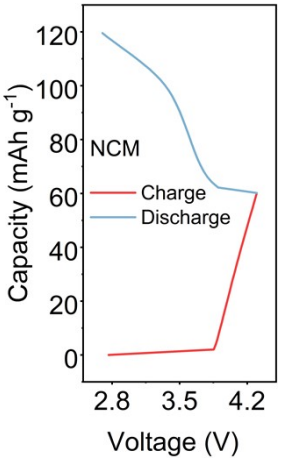

Figure S26. The charge-discharge profile of the NCM-based cell in a TMs-containing electrolyte (8 mM Mn $(TFSI)_2$+8 mM Ni $(TFSI)_2$ in 1 M EC/EMC electrolyte) during the initial cycle at 0.1 C.

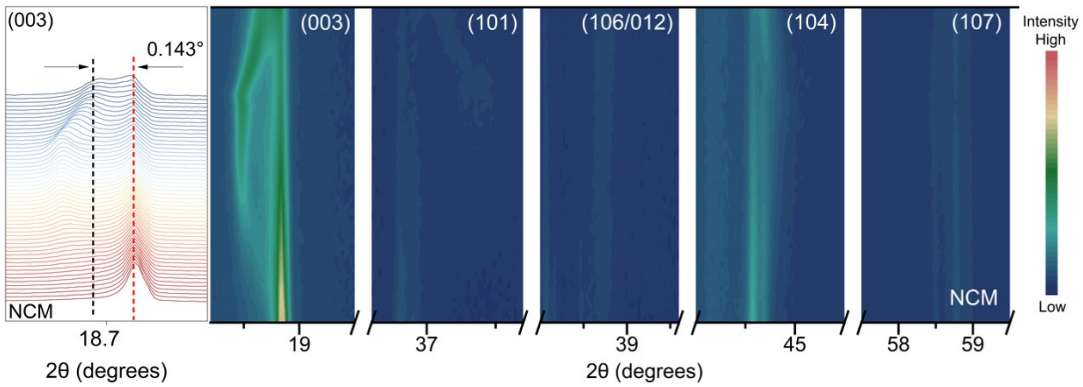

Figure S27. In situ-XRD patterns and contour plot of NCM-based cell cycled in a TMs-containing electrolyte.

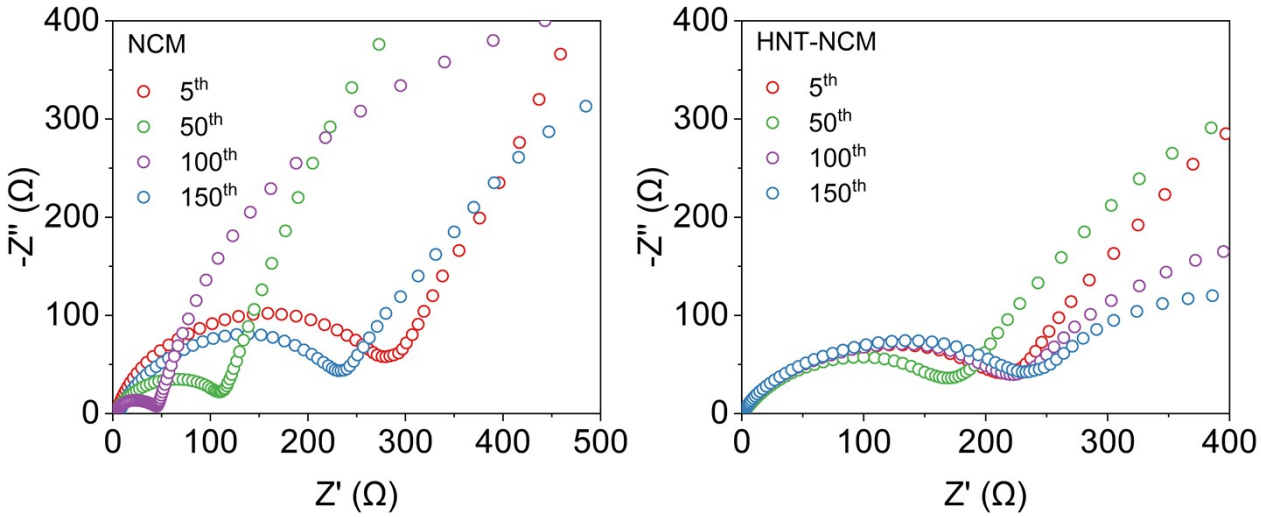

Figure S28. Nyquist plots for the NCM and HNT-NCM-based cells after different cycles.

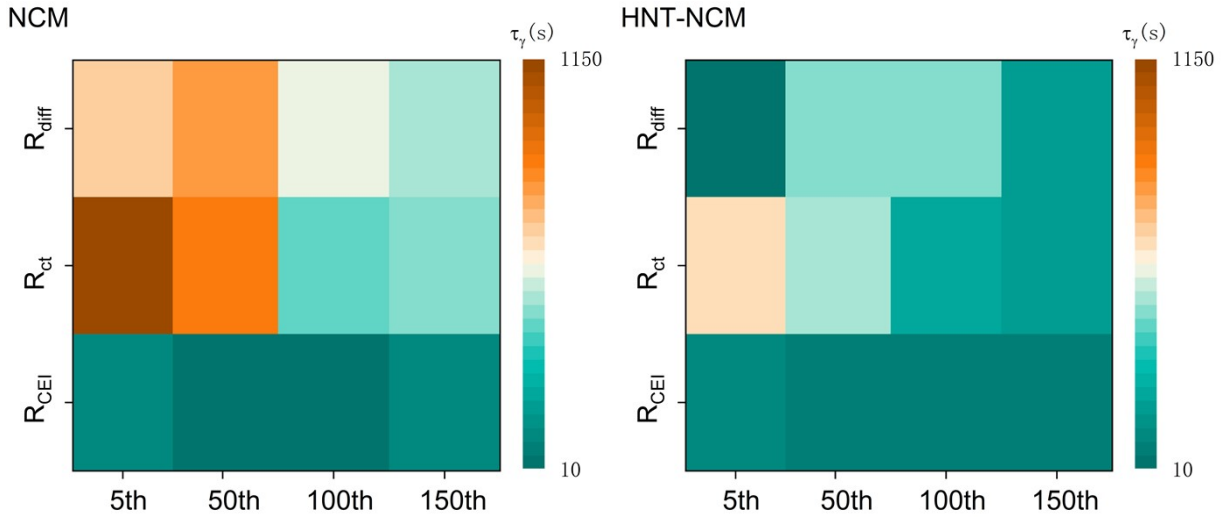

Figure S29. Relaxation time (τ_r) values assigned to the dissociated interfacial process with the NCM and HNT-NCM-based cells.

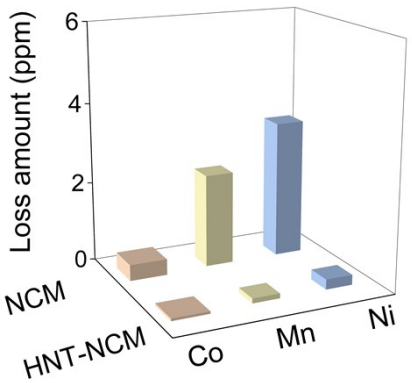

Figure S30. ICP-MS analysis of TMs dissolution in the electrolytes of the NCM//Li and HNT-NCM//Li cells after 100 cycles.

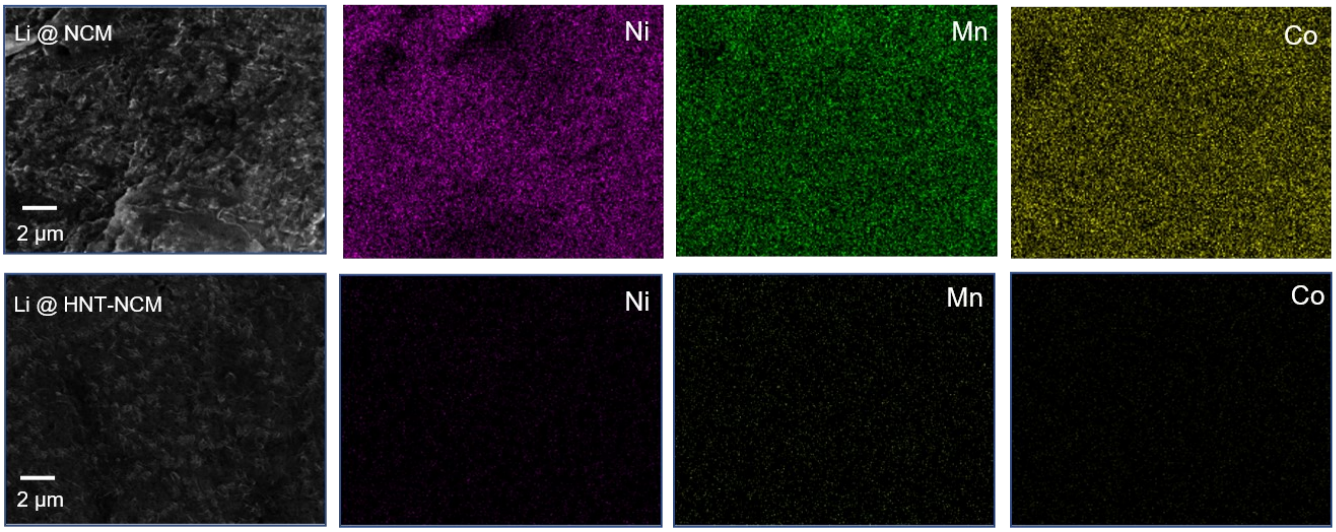

Figure S31. EDS mapping of Li metal anodes paired with the NCM or HNT-NCM cathode after 100 cycles.

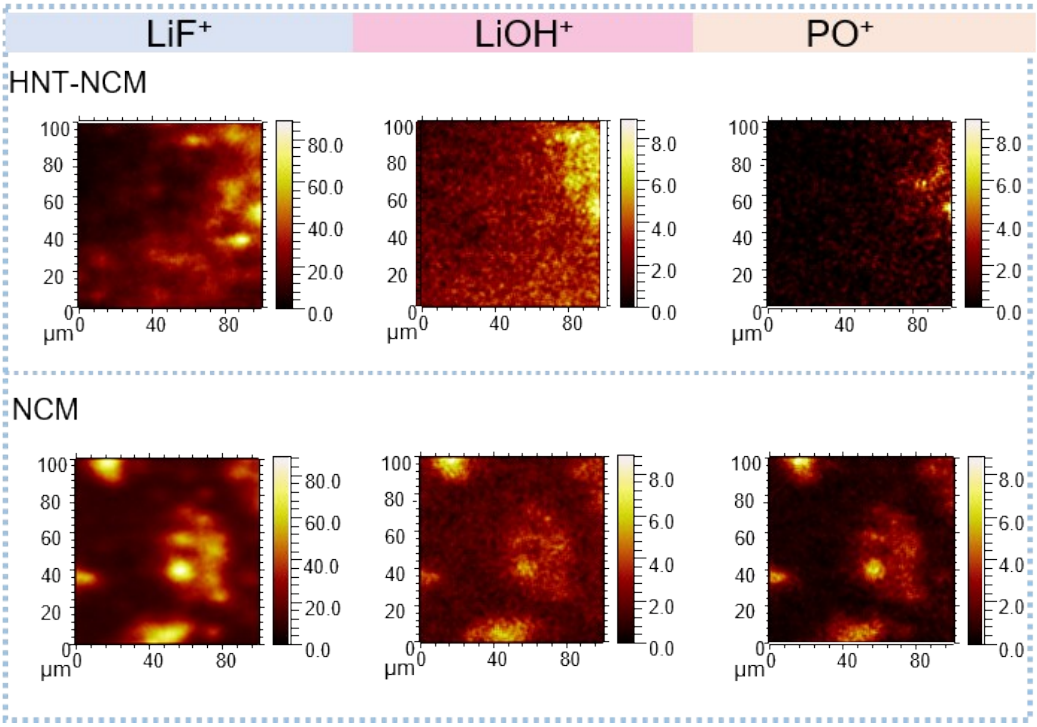

Figure S32. Surface species distributions (LiF^+, $LiOH^+$, and PO^+) on the Li anodes of NCM or HNT-NCM-based cells.

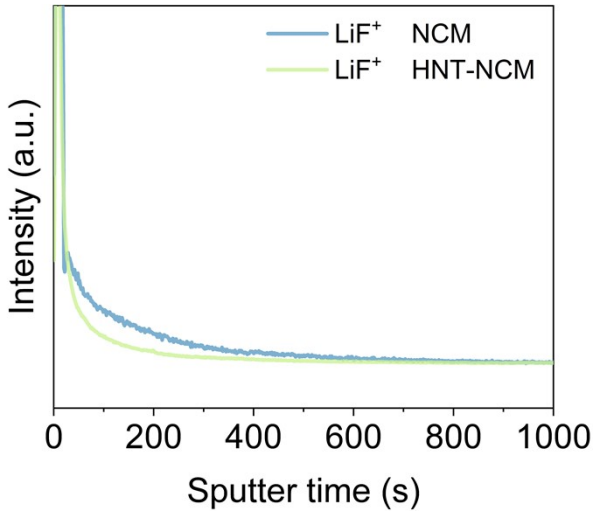

Figure S33. ToF-SIMS depth profiles of LiF^+ on the Li anodes of NCM or HNT-NCM-based cells.

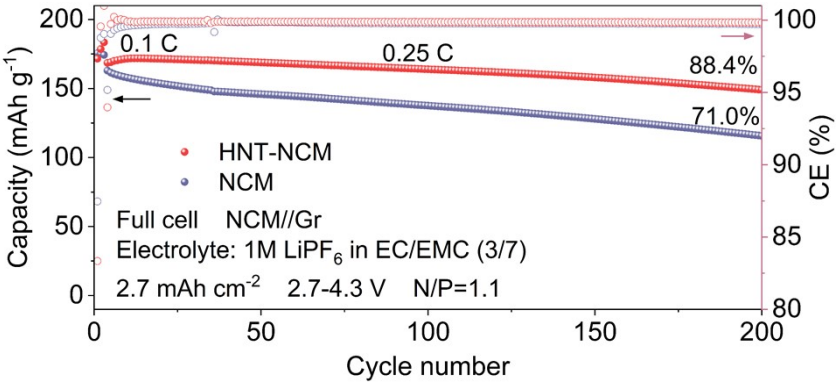

Figure S34. The cycling performance of the HNT-NCM//Gr full cell with an N/P ratio of 1.1 at 0.25 C.

Table S1. Comparison table of reported impurity-scavenging materials evaluated across different dimensional parameters.

Material	Ecofriendly	Availability	Reserves	Biocompatibility	Low cost
UiO-66-NH_2[1]	Involves toxic organic solvents	Complex modification	Zr: relatively stable reserves worldwide	Low	High synthesis cost
MIL-101(Cr)[2]	Environmental toxicity (Cr)	Widespread industrial use and strict treatment requirements	High	High	Cr: widely available and cheap
Zn-P-dmbIm[3]	Ligand synthesis is not environmentally friendly	Ligands are relatively rare	Rich and stable	Low, harmful to biological environments	High ligand price
Ti-MWW[4]	High	High	Rich	Low	Complex synthesis process
Halloysite [5 6]	Natural minerals are eco-friendly	High, widely distributed in nature	High, abundant reserves	High, Widely used in biomedicine	Low, clay: 0.04–0.12 US$ kg^{-1}[7]

Table S2. Comparison table of HNT with other clay minerals at different dimensionality scores.

Property	Halloysite	Sepiolite	Montmorillonite	Bentonite	Kaolinite	Zeolite
Mn ion adsorption (mg g^{-1})	3.10[8]	22.9[9]	3.22[10]	6.0[11]	0.446[12]	7.14[13]
Ni ion adsorption (mg g^{-1})	3.739[14]	12.15	2.1[15]	1.91[16]	2.47[17]	13.03[13]
Water adsorption	Middle	High (200 to 250% of its weight)[18]	High	High	Minimal	Low
Electrochemical stability	High: good electrochemical stability[19]	High: high chemical stability[20]	Low: swelling properties[21]	Low: swelling behavior[22]	High: non-water-swelling clays[23]	High: intrinsic chemical stability[24]
Surface charge (mV)	-35[25]	-50~-150[26]	-24.6~-37.4[27]	-30~-50[28]	-25~-41[29]	-36.1-38.3[30]

Table S3. Electrochemical performance comparison of our HNT-NCM cathode with other coating materials or additives.

Material	Cell	Cycling parameter	Capacity retention	References
Additives: 1% PFBNBS	Li//NCM622 (single-crystal)	75.2%@500 cycles	0.2 C@4.5 V@ 25 °C	*Adv. Funct. Mater.,* 2023, **33**, 2212150.
Lithium trifluoroacetate-lithium nitrate (LiTFA-$LiNO_3$) dual-salt additive	Li//NCM523 (polycrystalline)	80.2%@300 cycles	1 C@4.3 V@ 25 °C	*Angew. Chem. Int. Ed*., 2024, **63**, e202314876.
1% Al $(CF_3SO_3)_3$	Li//NCM811 (single-crystal)	91.5%@200 cycles	0.5 C@ 25 °C	*Adv. Funct. Mater.,* 2023, **33**, 2301642.
PR-co-PAA coating	Li//NCM@PR-co-PAA (polycrystalline)	86.2%@100 cycles	0.5 C@ 25 °C	*Adv. Mater.,* 2022, **34**, 2204835.
LTO ($Li_4Ti_5O_{12}$) coating	Li//R-NCM622-5% LTO (single-crystal)	79.3%@200 cycles	1 C@ 4.3 V@ 25 °C	*Adv. Funct. Mater.,* 2024, **35**, 2411182.
PEDOT skin coating	Li//NCM111 (polycrystalline)	91.1%@200 cycles	1 C@4.3 V@25 °C	*Nat. Energy*, 2019, **4**, 484-494.
Co_xB coating	Li//NCM811 (polycrystalline)	94.4%@200 cycles	0.5 C@4.4 V@ 25 °C	*Nat. Energy,* 2021, **6**, 362-371.
Silicon-doped	Li//Si-NCM9244 (polycrystalline)	72.5%@100 cycles	0.3 C@ 4.4 V @25 °C	*Adv. Energy Mater.,* 2022, **12**, 2200136
Halloysite additives	Li//NCM622 (single-crystal)	97.3%@300 cycles, 86.6%@500 cycles	2 C@4.3 V@25 °C	This work

Table S4. The parameters of the HNT-NCM-based pouch cell.

Pouch cell parameters	
Halloysite	**11.4 mg (3 wt.%)**
Cathode capacity	3.8 mAh cm^{-2}
Electrolyte	3.0 g Ah^{-1}, 180 mg
Anode	50 μm Li, 42.72 mg
Al foil	33.6. mg
Separator	16.3 mg
Cell capacity	60.8 mAh
N/P ratio	2.6
Energy density	348.5 Wh kg^{-1}

References

1 S. Mourdikoudis, S. Dutta, S. Kamal, S. Gómez-Graña, I. Pastoriza-Santos, S. Wuttke and L. Polavarapu, *Adv. Mater.*, 2025, **37**, 2415399.

2 C. Wang, S. Hou, M. Ma, Z. Ji, P. Wang, Y. Wang, Y. Su, Y. Zhou and M. Li, *J. Water Proc. Eng.*, 2024, **66**, 106040.

3 N. Ma, S. Kosasang, E. K. Berdichevsky, T. Nishiguchi and S. Horike, *Chem. Sci.*, 2024, **15**, 7474-7501.

4 Y. Wang, K. Wang, F. Wang, Y. Zhai, C. Bing, X. Fan, Q. Shen and X. Zhang, *Mater. Chem. Front.*, 2025, **9**, 8-29.

5 P. Yuan, D. Tan and F. Annabi-Bergaya, *Appl. Clay Sci.*, 2015, **112-113**, 75-93.

6 M. Liu, Z. Jia, D. Jia and C. Zhou, *Prog. Polym. Sci.*, 2014, **39**, 1498-1525.

7 K. G. Bhattacharyya and S. S. Gupta, *Adv. Colloid Interface Sci.*, 2008, **140**, 114-131.

8 P. Mishra, L. Kaur, R. Patel, R. K. Mishra, D. K. Verma and W. Daoudi, *J. Environ. Chem. Eng.*, 2024, **12**, 114611.

9 S. Kocaoba, *Desalination*, 2009, **244**, 24-30.

10 O. Abollino, M. Aceto, M. Malandrino, C. Sarzanini and E. Mentasti, *Water Res.*, 2003, **37**, 1619-1627.

11 J. S. Al-Jariri, F. J. D. Khalili and W. *Treatment*, 2010, **21**, 308-322.

12 Ö. Yavuz, Y. Altunkaynak and F. Güzel, *Water Res.,* 2003, **37**, 948-952.

13 S. R. Taffarel and J. Rubio, *Miner. Eng.*, 2009, **22**, 336-343.

14 D. Le Thi, L. T. P. Thao, D. Cong Tien, H. Nguyen Viet, H. Ha Manh, T. Mai Van, T. Nguyen Thi Thanh and B. Bui Hoang, *Vietnam J. Sci. Technol.*, 2024, **62**, 965-978.

15 S. Sen Gupta and K. G. Bhattacharyya, *Phys. Chem. Chem. Phys.*, 2012, **14**, 6698-6723.

16 M. G. A. Vieira, A. F. A. Neto, M. L. Gimenes and M. G. C. da Silva, *J. Hazard. Mater.*, 2010, **177**, 362-371.

17 K. G. Bhattacharyya and S. S. Gupta, *Appl. Clay Sci.*, 2008, **41**, 1-9.

18 A. K. Helmy and S. G. de Bussetti, *Appl. Surf. Sci.*, 2008, **255**, 2920-2924.

19 N. Pandi, S. H. Sonawane, A. K. Kola, U. K. Zore, P. H. Borse, S. B. Ambade and M. Ashokkumar, *Energy Ecol. Environ.*, 2021, **6**, 13-25.

20 S. Martinez-Ramirez, F. Puertas and M. T. Blanco-Varela, *Clay Miner.*, 1996, **31**, 225-232.

21 J. Peng, H. Yi, S. Song, W. Zhan and Y. Zhao, *Results in Phys.*, 2019, **12**, 113-117.

22 M. Alzamel, M. Fall and S. Haruna, *J. Rock Mech. Geotech.*, 2022, **14**, 689-702.

23 D. Turer, *Environ. Geol.*, 2007, **52**, 421-425.

24 X. Chi, M. Li, J. Di, P. Bai, L. Song, X. Wang, F. Li, S. Liang, J. Xu and J. Yu, *Nature*, 2021, **592**, 551-557.

25 H. Zhang, *Nanotechnology Rev.* **2017**, *6*, 573-581.

26 N. Tekin, A. Dinçer, Ö. Demirbaş and M. Alkan, *J. Hazard. Mater.*, 2006, **134**, 211-219.

27 Y. Yu, L. Ma, H. Xu, X. Sun, Z. Zhang and G. Ye, *Powder Technol.*, 2018, **330**, 147-151.

28 M. H. Baik and S. Y. Lee, *J. Ind. Eng. Chem.*, 2010, **16**, 837-841.

29 Y. Yukselen and A. Kaya, *Water Air Soil Poll.*, 2003, **145**, 155-168.

30 W. Shi, F. Gao, X. Li and Z. Wang, *Water Res.*, 2022, **221**, 118849.